A methodology for modeling photocatalytic reactors for indoor pollution control using previously estimated kinetic parameters

Claudio Passalía [a,b], Orlando M. Alfano [a,b], Rodolfo J. Brandi [a,b,∗]

[a] INTEC – Instituto de Desarrollo Tecnológico para la Industria Química, CONICET – UNL, Güemes 3450, 3000 Santa Fe, Argentina
[b] FICH – Departamento de Medio Ambiente, Facultad de Ingeniería y Ciencias Hídricas, Universidad Nacional del Litoral, Ciudad Universitaria, 3000 Santa Fe, Argentina

ARTICLE INFO

ABSTRACT

A methodology for modeling photocatalytic reactors for their application in indoor air pollution control is carried out. The methodology implies, firstly, the determination of intrinsic reaction kinetics for the removal of formaldehyde. This is achieved by means of a simple geometry, continuous reactor operating under kinetic control regime and steady state. The kinetic parameters were estimated from experimental data by means of a nonlinear optimization algorithm.

The second step was the application of the obtained kinetic parameters to a very different photoreactor configuration. In this case, the reactor is a corrugated wall type using nanosize TiO_2 as catalyst irradiated by UV lamps that provided a spatially uniform radiation field. The radiative transfer within the reactor was modeled through a superficial emission model for the lamps, the ray tracing method and the computation of view factors. The velocity and concentration fields were evaluated by means of a commercial CFD tool (Fluent 12) where the radiation model was introduced externally. The results of the model were compared experimentally in a corrugated wall, bench scale reactor constructed in the laboratory. The overall pollutant conversion showed good agreement between model predictions and experiments, with a root mean square error less than 4%.

© 2011 Elsevier B.V. All rights reserved.

1. Introduction

Regarding air pollution, the social concern has been usually focused on outdoor air quality problems. Nevertheless, in the past decades, along with the improvement of living standard, there has been an increasing interest in the role played by indoor or confined environments pollution in human health [1,2]. This is due to a conjunction of three main factors: (a) modern buildings tend to be designed and constructed with a high thermal insulation and air tightness in order to optimize the air conditioning processes and thus save energy and money [3]; (b) there are a large number and types of materials found indoors that may release chemical compounds into their surroundings and which can reach unhealthy concentrations; (c) the fact that, in most societies, people spend far more time doing activities indoors rather than outside [4]. In addition to the aforementioned factors, it should be added that many studies have demonstrated that for some compounds, indoor concentrations can be higher than outside [5,6]. Moreover, this indoor pollution presents a more difficult detection compared to the typically particulate-matter-related urban pollution [7].

The effects in human health of a poor air quality in a room depend on the type and concentration of pollutant, exposure times and the genetic predisposition of the occupants. A generalized clinical picture that combines headaches, nausea, dizziness, eye, nose, or throat irritations, dry cough and tiredness [8] is known as Sick Building Syndrome (SBS). This syndrome is usually associated with the presence of volatile organic compounds (VOCs) [1,3].

Indoor air pollution may be a result of in situ generation or from an exchange with the outside. Indoor chemical pollutants, particularly VOCs, are emitted from building materials, furniture and equipment [8]. Among VOCs, formaldehyde (HCHO) is one of the most dominant and has a particular interest due to its abundance in an indoor environment [4,6]. HCHO is usually the most abundant aldehyde in air and also the most studied [5].

HCHO is the simplest aliphatic aldehyde; at ordinary temperatures, HCHO is a strong smelling colorless gas. It is a widely used chemical in the industry and is present in a large number of household items, such as furnishing, carpeting, paints and cleaning products; it is also a byproduct of some combustion processes, like incense sticks and cigarettes [2,6]. Indoor concentrations of HCHO may reach up to 2 ppmv (1 ppmv = 1.23 mg m^{-3} @NTP), but are typically below 0.1 ppmv [1]. In this range, gaseous HCHO is known to

Nomenclature

A_{cat}	photocatalytic area (cm^2)
C	molar concentration (mol cm^{-3})
ΔF_{ij}	view factor (dimensionless)
D_{Fm}	molecular diffusivity of formaldehyde in a mixture (cm^2 s^{-1})
$e^{a,sup}$	local superficial rate of photon absorption, LSRPA (einstein cm^{-2} s^{-1})
g	gravitational acceleration (cm s^{-2})
H_{ij}	visibility factor (dimensionless)
I	specific radiation intensity (einstein cm^{-2} s^{-1} sr^{-1})
J	diffusive molar flux (mol cm^{-2} s^{-1})
K_W	kinetic parameter (cm^3 mol^{-1})
L_L	lamp useful length (cm)
N	total molar flux (mol cm^{-2} s^{-1})
$\underline{n}$	unit outwardly directed normal to the catalytic plane (dimensionless)
P	pressure (dyn cm^{-2}); also lamp power output (einstein s^{-1})
q	radiation flux (einstein cm^{-2} s^{-1})
Q	volumetric flow rate (cm^3 s^{-1})
r_F	heterogeneous reaction rate (mol cm^{-2} s^{-1})
r_L	lamp radius (cm)
R	homogeneous reaction rate (mol cm^{-3} s^{-1})
R_λ	spectral reflectance
T_λ	spectral transmittance
v	velocity (cm s^{-1})
x, y, z	coordinate system
X	conversion (dimensionless)

Greek letters

α	kinetic parameter (cm^3 einstein^{-1})
ρ	density (g cm^{-3})
η_λ^{abs}	fraction of spectral radiation absorbed (dimensionless)
κ_F	kinetic parameter (cm^3 mol^{-1})
λ	wavelength (nm)
$\underline{\underline{\tau}}$	viscous stress tensor
ϕ, θ	spherical coordinates (rad)

Subscripts

cat	relative to a catalytic wall
exp	relative to experimental data
mod	relative to model
non-cat	relative to a non catalytic wall
F	relative to formaldehyde
Fi	relative to a radiation filter
W	relative to water
w	relative to wall
wi	relative to reactor window
λ	wavelength dependence

Superscripts

abs	absorption of radiation
in	relative to reactor inlet; also, relative to incoming radiation flux
out	relative to outgoing radiation flux

Special characters

$\_$	denotes a vector
$\langle \rangle$	indicates an averaged property

produce headache, nausea and chest tightness; it can also irritate the eyes and the respiratory tract and skin [4]. This concentration range, unfortunately, is in perfect accordance with the odor threshold of HCHO. For higher levels, between 5 and 30 ppmv, HCHO can produce irritation of lower airway and pulmonary effects [1,4]. Furthermore, HCHO was recently categorized as a human carcinogen [9].

Due to the unhealthy impact of HCHO presence inside buildings and its ubiquity, there is a serious need to attain its abatement. Traditional approaches to reduce exposure are related to source control, increasing of air renewal rates and air cleaning. When the two first are not possible to carry out, an air treatment technique must be applied. Conventional control processes, such as filtration and adsorption, have major drawbacks, mainly due to the low concentrations of pollutants and also the final disposal requirements. In this context, gas phase heterogeneous photocatalysis appears as an emerging technology for indoor air purification.

Photocatalytic devices for purification of indoor air have already been probed with success in the elimination of a wide range of organic and inorganic pollutants [10–13]. The technology relies on the properties of TiO$_2$ nanoparticles, a semiconductor that, under the illumination of UV light, can start a series of surface reactions leading to the complete mineralization of the pollutant. The main advantages of this technology also include: the operation at room temperature and atmospheric pressure, the use of an inexpensive catalyst and the possibility of combination with conventional control devices [2,3,14].

Photocatalytic processes have been intensively investigated, addressing issues such as reaction kinetics, doping and deactivation of photocatalyst, and reactor design [14]. Among the pollutants studied, HCHO is not an exception. The photocatalytic degradation of gaseous HCHO has already been addressed in a number of works that probed the feasibility of its elimination [2,3,10,15].

Chemical processes involving simultaneously momentum, heat, mass and radiation transfer usually need an optimization of the reaction unit in order to obtain the best result regarding overall performance, space and economic restraints and radiation usage. The recognition of the scale dependency of these processes is crucial. The mathematical simulation and prediction of otherwise expensive and time consumptive physical prototypes is a very helpful tool. This is especially true nowadays that the computational capabilities are sufficiently large to provide a detailed approach of every phenomena involved. In particular, CFD tools have been increasingly used to model very different kinds of processes, including photocatalytic reactions. In particular, there have been valuable contributions in the CFD modeling approach for gas phase photocatalytic reactors [16–18].

In this work, we deal with the study of photocatalytic reactors for their application in air pollution remediation. The target pollutant selected was HCHO. The study approach is based on the application of experimentally determined kinetic parameters in the modeling of a complex geometry reactor. To this aim, the first step consists in the construction and operation of a small, simple geometry reactor to perform a series of experiments and obtain the kinetic parameters. Once the kinetic parameters are known, they are able to be used in a very different reactor configuration, such as the corrugated plate type coated with TiO$_2$ as catalyst. The approach of radiation interchange between catalytic walls makes use of geometrical configuration factors; a study of the influence of catalyst layers optical properties on the radiation interchange was also made. The modeling of this corrugated photocatalytic reactor was performed using a commercial CFD package.
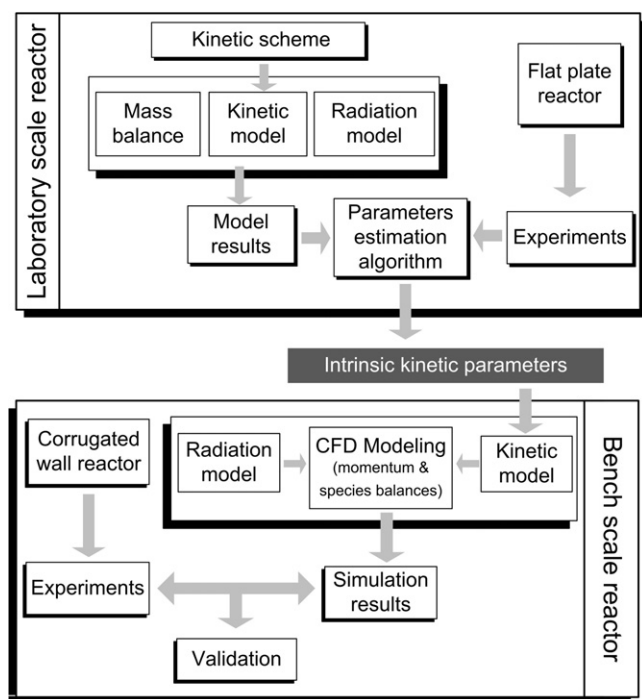
Fig. 1. Scaling methodology.

Table 1
Main characteristics of reactors.

	Description	Values
Laboratory reactor	Effective volume	$25.6\,cm^3$
	Dimensions	$8\,cm \times 8\,cm \times 0.4\,cm$
	Lamps	5
	Catalytic area	$64\,cm^2$
Corrugated wall reactor	Total volume	$1800\,cm^3$
	Lamps	10
	Catalytic area	$1843.5\,cm^2$
	Number of channels	17
	Folded angle	$57°$
Operating conditions	Temperature	$25\,°C$
	Inlet HCHO concentration	5–35 ppmv
	Relative humidity	10–75%
	Maximum radiation	8.94×10^{-9} einstein $cm^{-2}\,s^{-1}$
	Radiation levels	16, 26, 60, 100%
UV Lamps	Type	Sylvania F15W T12
	Nominal power	15 W
	Dimensions	$r_L = 1.78$ cm, $L_L = 43$ cm
	Emission peak	352 nm

2. Methodology

The main objective of the present work is to implement a methodology for the modeling of a photocatalytic reactor using experimental data obtained in a simple geometry, laboratory scale reactor. The kinetic model developed in the previous step is then employed in the scaling of the photocatalytic process, which allows predicting the performance of a different size and configuration bench scale reactor.

The intrinsic kinetics to be obtained implies the independence of reactor design variables, including the radiation source and operating variables. To this aim, the methodology implies two keystone points: (i) to employ the same catalyst immobilization technique in both reactors; (ii) to ensure that the experimental data in the laboratory reactor are obtained under kinetic control regime to eliminate the effect of mass transfer limitations. The employed methodology for this scaling-up, which is schematically represented in Fig. 1, may be summarized in the following steps:

Firstly, using a plausible reaction scheme for the photocatalytic degradation of the chosen compound, an analytical reaction rate expression is derived. In this particular case, the HCHO photodegradation reaction depends on the stable species (HCHO and H_2O) local concentrations and the Local Superficial Rate of Photon Absorption (LSRPA or $e^{a,sup}$). On the other hand, a mathematical model for the laboratory reactor must be stated. Such a model is derived from accurate mass balances and the radiation field inside the reactor. The latter, required to establish the effect of radiation absorption on the reaction rate, is evaluated by a radiative transfer model, which includes an emission model for the lamps and the determination of spectral optical properties.

When the reactor model is coupled with the kinetic expressions, the laboratory reactor can be precisely simulated. By introducing the experimental data into the simulations, the unknown kinetic parameters may be determined. The estimation of the kinetic parameters is achieved by applying a nonlinear optimization algorithm to fit the model predictions to the experimental data.

Once the reaction kinetic expression and the corresponding kinetic parameters are known, its application to any reactor configuration or shape is straightforward, provided that: the reactor mass balances can be solved, the catalyst is immobilized by the same protocol and, last but not least, the radiation field can also be evaluated properly. Thus, the radiation transfer equation must be applied to the new reactor in order to predict the local photon absorption rate, which may differ from the laboratory one not only in size or shape, but also in the way it is irradiated. The obtained field of $e^{a,sup}$ is introduced in the mass balance to simulate the reactor performance and predict its conversion.

Finally, data obtained from experimental runs in the bench scale reactor are contrasted against simulation results in order to validate the procedure. Similar methodology approaches can be found in Mohseni and Taghipour [16], Imoberdorf et al. [13] and Queffeulou et al. [19]. However, in the present work, a radiation interchange model between catalytic walls is developed using geometrical configuration factors. Besides, the effects of the catalyst layer optical properties on this radiation interchange are studied.

2.1. Experimental set-up and procedures

A complete experimental device was designed and constructed (Fig. 2), the core of which being, in each case, the photoreactor itself. Both reactors were made of acrylic (walls and windows) and stainless steel as a support for the TiO_2 catalyst. More details on reactors dimensions and operating conditions are included in Table 1.

The special acrylic material used to build the reactor windows is transparent to radiation of wavelengths in the near UV range (300–400 nm), the useful radiation band for the TiO_2 photoactivity.

Radiation was supplied by a set of tubular black light fluorescent lamps facing the reactor window. The lamps are positioned with their axes parallel to each other but at different distances from the window. The lamps in the extremes of the set (lamps I and V) were brought closer and the central lamp (lamp III) was moved away. This non-aligned arrange provides a nearly uniform incident radiation flux over the coated area of the plate. Neutral optical filters made with metal meshes were interposed between the radiation emitting system and the reactor to modify the level of incident radiation.

The polluted air entering the reactor consists of three different streams that are mixed: a purified dry air current, a water vapor saturated stream and a formaldehyde enriched air. The latter is obtained by on-line generation of monomeric gaseous formaldehyde by controlled sublimation of paraformaldehyde (Aldrich, reagent-grade). Formaldehyde concentrations in air were
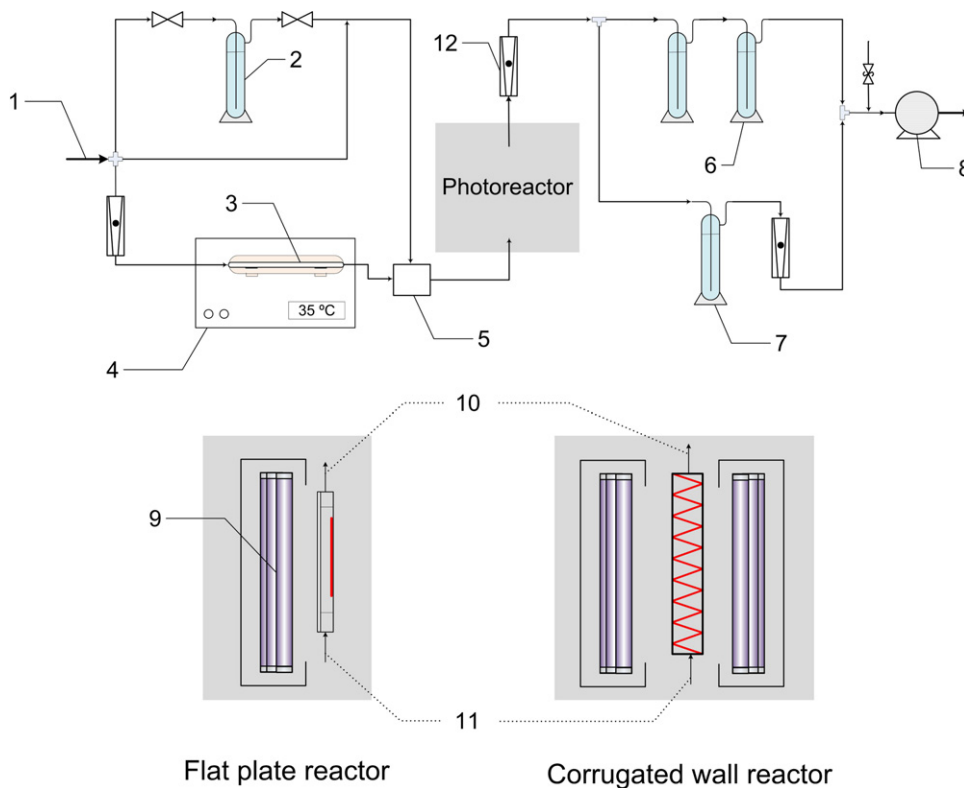
Fig. 2. Experimental layout of reactors: (1) purified dry air entrance; (2) humidifier; (3) formaldehyde generator; (4) thermostatic bath; (5) feed flow junction; (6) scrubbers; (7) sample collector; (8) pump; (9) UV lamps; (10) reactor outlet; (11) reactor inlet; and (12) flow meter.

determined using a standard method [20]. The concentrations of HCHO at the reactor inlet ranged from 5 to 35 ppmv. A vacuum pump at the end of the system provides the air circulation. A clean dry air current is obtained by passing air through activated carbon and silica gel columns. Volumetric flow rates in the system were measured using variable area flow meters. All conduits are made of stainless steel and PTFE.

The experimental device admits to take samples only at the reactor outlet. Hence, C_F^{in} is determined with samples taken with occluded lamps; when a steady state concentration is achieved, the lamps are uncovered. Then, during the irradiated period, samples are taken until HCHO concentration reaches a new steady state, the outlet concentration (C_F^{out}). Finally, the lamps are turned off and it is checked that the inlet concentration is unchanged.

The effect of radiation level on the HCHO reaction rate was evaluated using a set of neutral optical filters between the lamps and the reactor window. They consisted of stainless steel meshes hold by a frame, which provided a grey attenuation in the radiation over the 300–400 nm range. The radiation levels are summarized in Table 1.

3. Laboratory scale reactor

The kinetic study was conducted in a laboratory scale, flat plate photocatalytic wall reactor. It operates in a continuous way with a single pass. The reactor geometry consists of a rectangular parallelepiped formed by the walls, window and TiO$_2$ coated stainless steel. The effective reactor volume is 25.6 cm^3 through which a contaminated air stream is circulated. A series of small orifices was placed at the reactor inlet in order to obtain a well distributed flow and concentration profiles in the cross section of the reactor. Further details on the reactor, its modeling and results can be found in a previous work [21].

A simple mass balance for the reactor was formulated. The expression for the heterogeneous reaction rate, r_F, was derived

analytically from a proposed mechanism; the resulting expression was

$$r_F = \frac{-\alpha e^{a,sup} C_F}{1 + K_W C_W + \kappa_F C_F} \tag{1}$$

The lumped kinetic parameters are combinations of kinetic constants, concentrations of species that remain inalterable or considered in excess, and adsorption equilibrium constants that relate bulk to surface concentrations. In order to obtain intrinsic parameters for the degradation kinetics, the experimental data were obtained under kinetic control regime, i.e., in the absence of mass transfer limitations. These data were used as inputs in the numeric parameter estimation. By combination of the mass balance with the expression for the reaction rate [Eq. (1)], an implicit expression is analytically obtained:

$$\kappa_F \left(C_F^{out} - C_F^{in} \right) + (1 + K_W C_W) \ln \left(\frac{C_F^{out}}{C_F^{in}} \right) = -\alpha \frac{A_{cat}}{Q} e^{a,sup} \tag{2}$$

where C_F^{in} and C_F^{out} are, respectively, the inlet and outlet concentrations of formaldehyde, Q is the volumetric flow rate and A_{cat} is the photocatalytic area. Eq. (2) was used to evaluate the three kinetic parameters, namely α, κ_F and K_W. The optimization procedure to obtain the values of the kinetic parameters in Eq. (2) was a nonlinear algorithm that used the matrix of experimental data containing (i) HCHO inlet concentrations, (ii) relative humidities, (iii) radiation levels and (iv) outlet HCHO concentrations. The values and units of the estimated parameters are: $\alpha = 1.34 \times 10^8$ (cm^3 einstein^{-1}); $\kappa_F = 7.17 \times 10^9$ (cm^3 mol^{-1}) and $K_W = 2.97 \times 10^6$ (cm^3 mol^{-1}) [21].
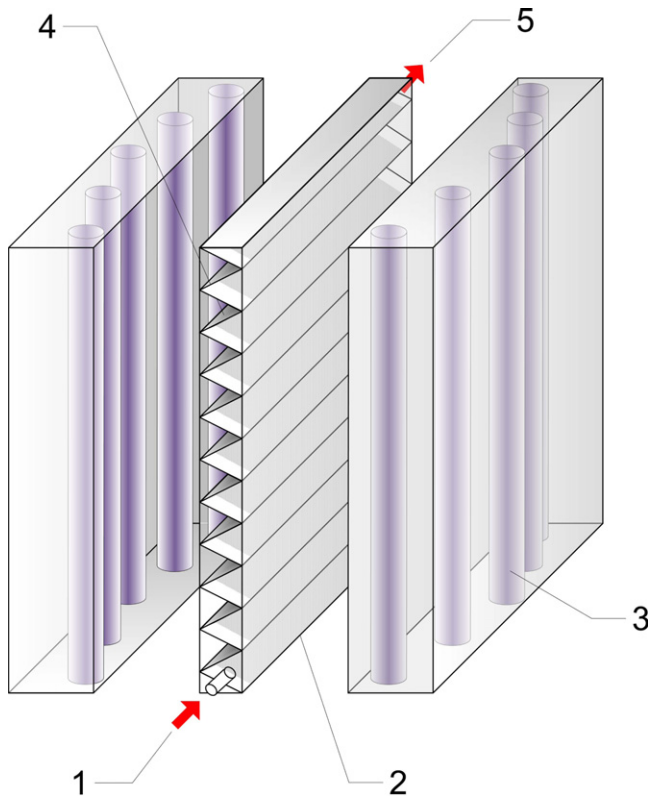
Fig. 3. Corrugated reactor scheme: (1) air inlet; (2) reactor window; (3) UV lamps; (4) TiO$_2$ coated stainless steel; and (5) air outlet.

4. Corrugated wall reactor

4.1. Reactor characteristics and set-up

The complete experimental set-up, except for the photoreactor, was the same as described in Section 3. The bench scale photocatalytic reactor consists of a stainless steel corrugated plate coated with TiO$_2$ and placed inside an acrylic frame. The reactor was irradiated by two sets of five black light tubular lamps positioned in a non-aligned arrange (Fig. 3). Such an arrangement provides a uniform radiation flux on the reactor window.

The corrugated reactor is continuous and single-pass. The stainless steel plate was folded into 57° angle (1 radian) triangular channels. Inside the reactor, air flows in a zigzag pattern from one channel to another. The gaseous stream entering the reactor consists of a HCHO-polluted air with a given amount of water vapor. The total volumetric flow rate was set to 3.5 L/min.

4.2. Reactor modeling

4.2.1. Conservation equations

The modeling of velocity and concentration fields in the corrugated reactor was achieved using a CFD software. The heterogeneous reacting system was studied under isothermal and steady state conditions. Air is considered a Newtonian incompressible fluid with constant physical properties and with a laminar flow regime (the calculated Reynolds number is 140). Under these assumptions, the CFD modeling consists in the resolution of the continuity, Navier–Stokes and conservation of species equations:

$$\underline{\nabla} \cdot (\rho \underline{v}) = 0 \tag{3}$$

$$\underline{\nabla} \cdot (\rho \underline{v}\underline{v}) = -\nabla P + \underline{\nabla} \cdot (\underline{\underline{\tau}}) + \rho \underline{g} \tag{4}$$

$$\underline{\nabla} \cdot (\rho \underline{v} C_i) = -\underline{\nabla} \cdot \underline{J}_j + R_i \tag{5}$$

where ρ is the fluid density, $\underline{v}$ the velocity, P the pressure, $\underline{\underline{\tau}}$ the viscous stress tensor, g the gravitational acceleration, C_i the molar concentration of species i, J_j the diffusion flux vector and R_i the rate of production or depletion of species i by homogeneous chemical reaction. Newton's law of viscosity was introduced into Eq. (4) as a constitutive equation for the definition of the stress tensor. As there are no homogeneous reactions in the system, the term R_i in Eq. (5) is zero for every species i.

4.2.2. Boundary conditions

Every wall was set as stationary with no slip shear condition. A velocity magnitude normal to the boundary and the HCHO and water vapor mass fractions were specified as boundary conditions at the reactor inlet.

Heterogeneous reaction appears in the balance as a boundary condition. For catalytic walls (A_{cat}) the diffusive HCHO molar flux must be equal to the heterogeneous reaction rate:

$$\underline{n} \cdot \underline{N}_F|_{A_{cat}} = \underline{n} \cdot (-D_{Fm} \underline{\nabla} C_F)|_{A_{cat}} = r_F \tag{6}$$

On the other hand, for the non reactive walls ($A_{non\text{-}cat}$), a zero molar flux for any species was specified.

$$\underline{n} \cdot \underline{N}_F|_{A_{non\text{-}cat}} = 0 \tag{7}$$

The heterogeneous reaction rate in Eq. (6), r_F, was introduced into the CFD solver as a user defined function (UDF). This reaction rate was evaluated as a function of the local reactant concentrations and the LSRPA.

4.2.3. Radiation field model

Besides the boundary conditions for the HCHO mass balance, there is also need for evaluating the radiation boundary condition, i.e., the radiation entering the reactor through the windows. In its turn, this entering radiation determines the $e^{a,sup}$ on the catalytic walls, which is introduced into Eq. (1) to compute r_F; this result is then replaced on the right hand side of Eq. (6). The computation of the radiation field inside the reactor to obtain the LSRPA includes the superficial emission model for the lamps and the ray tracing method. This allows the integration of radiation contributions coming from any point at the lamps surface that is visible from the point of incidence considered on the catalytic film (plane $X = 0$). The specific radiation intensity given by the superficial emission model is

$$I_\lambda(y, z, \phi, \theta) = T_{\lambda,Wi} T_{\lambda,Fi} I_{0,\lambda} = T_{\lambda,Wi} T_{\lambda,Fi} \frac{P_\lambda}{2\pi^2 r_L L_L} \tag{8}$$

where ϕ and θ are spherical coordinates whose origin is the point of incidence, $T_{\lambda,Wi}$ is the transmittance of the reactor window, $T_{\lambda,Fi}$ is the transmittance of the neutral optical filter, $I_{0,\lambda}$ is the outgoing radiation at the lamps surface, P_λ is the emission power output of the lamp, and r_L and L_L are, respectively, the lamp radius and useful length.

Apart from that, for this multilamp system, the additive effect of each lamp on the radiation flux must be taken into account. Consequently, the expression of the radiation flux entering the reactor, q_n^{Wi}, is given by

$$q_n^{Wi}(y, z) = \sum_\lambda T_{\lambda,Wi} T_{\lambda,Fi} \sum_i \int_{\phi_{1,L_i}}^{\phi_{2,L_i}} \int_{\theta_{1,L_i}}^{\theta_{2,L_i}} \frac{P_{\lambda,L_i}}{2\pi^2 r_{L_i} L_{L_i}} \sin^2\theta \sin\phi \, d\theta \, d\phi \tag{9}$$

where ϕ_{1,L_i}, ϕ_{2,L_i}, θ_{1,L_i}, θ_{2,L_i} are the limiting angles from which radiation can reach the incidence point for the lamp i. This radiation flux was numerically evaluated by means of a specifically written Fortran code that solves Eq. (9).

Due to the presence of radiation in the system, Eqs. (3)–(7) are not enough to model the corrugated wall reactor completely.
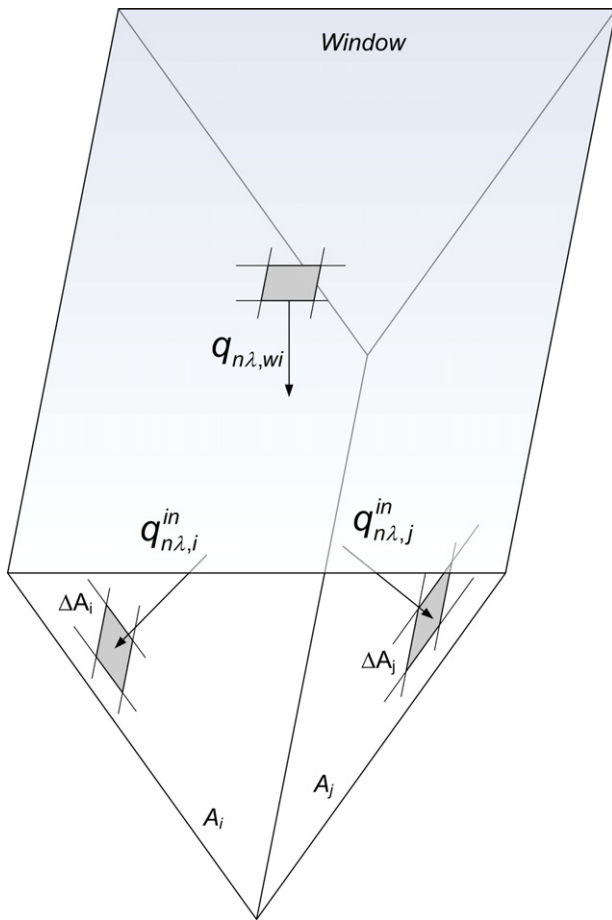
Fig. 4. Radiation fluxes in the triangular channel.

Radiative fluxes and interactions between surfaces are needed in this case, where reflection, transmission and absorption are involved.

The radiation interchange can be modeled considering a triangular prism with two catalytic walls, the remaining being the reactor window (Fig. 4). The window is taken as an emitting surface, though strictly it only lets in the radiation coming from the lamps. The radiation flux emitted by the transparent surface is assumed uniform for each channel. The catalytic walls are opaque and therefore do not transmit radiation, but they can reflect and absorb radiation. Both the reflected radiation on the catalyst surface and the emitted by the transparent window are considered diffuse. At every catalytic surface position, radiation flux ($q_{n\lambda,i}$) may come directly from the window ($q_{n\lambda,i}^{in,wi}$) and indirectly by reflection on the opposite catalytic surface ($q_{n\lambda,i}^{in,wall}$).

Each surface is divided into small rectangular flat elements to compute the LSRPA. Elements in the same plane are not visible to each other and therefore do not interact. In addition, due to the channel symmetry, the radiation field on one catalytic surface is the specular image of the distribution in the opposite catalytic wall. As the catalyst is uniformly distributed, absorbed fraction (η_λ^{abs}) and reflected fraction (R_λ) do not depend on the position.

The radiation flux that reaches an element i of one of the catalytic surfaces from the reactor window can be calculated as

$$q_{n\lambda,i}^{in,wi} = q_{n\lambda,wi} \Delta F_{i,wi} \tag{10}$$

Besides, the radiation flux incident on an element i from the other catalytic surface can be evaluated from the following expression:

$$q_{n\lambda,i}^{in,wall} = \sum_{j}^{N_j} \left[\left(R_\lambda q_{n\lambda,j}^{in} \right) H_{i,j} \Delta F_{ij} \right] \tag{11}$$

where H_{ij} is a visibility factor between elements i and j. This visibility factor takes the value of 0 if elements i and j are on the same plane and 1 in any other case. ΔF_{ij} is the view factor between two differential areas, defined as

$$\Delta F_{ij} = \frac{\cos \theta_j \cos \theta_i}{\pi \ r_{ij}^2} \Delta A_j \tag{12}$$

Here $q_{n\lambda,i}^{in}$ is the incoming radiation flux over the surface element i and $q_{n\lambda,wi}$ the radiation flux emitted by the window. Under these considerations, an algebraic linear system results as a model for the radiation interaction between surface elements:

$$q_{n\lambda,i}^{in} - \sum_{j}^{N_j} \left[\left(R_\lambda \ q_{n\lambda,j}^{in} \right) H_{ij} \Delta F_{ij} \right] = q_{n\lambda,wi} \Delta F_{i,wi} \tag{13}$$

The radiation fluxes involved in Eq. (13) are schematically shown in Fig. 4. On the other hand, the LSRPA for a surface element on a catalytic wall is

$$e^{a,sup} = \sum_{\lambda} e_{\lambda}^{a,sup} = \sum_{\lambda} \eta_{\lambda}^{abs} q_{n\lambda}^{in} \tag{14}$$

where η_λ^{abs} is the fraction of absorbed radiation. A more general radiation interchange model can be found elsewhere [22].

In order to solve Eqs. (13) and (14), the optical properties of the catalytic surfaces ($R_{\lambda,j}$ and η_λ^{abs}) must be known, as well as the net flux of radiation "emitted" by the window ($q_{n\lambda,wi}$).

The modeling of radiation flux was evaluated and introduced into the CFD solver as a boundary condition through user defined functions (UDFs). Due to the spatial distribution of the lamps, the "emitted" radiation flux is nearly uniform over the catalytically active zone of the reactor. The flux is symmetrical respect to the centre of the window, where the radiation flux has its maximum values.

A study was performed to evaluate the influence of the catalyst layer optical properties on the global radiation interchange. To this aim, the spectral fractions of reflected and absorbed radiation were determined for different deposition cycles over the stainless steel plate. The spectral optical properties involved in the modeling were experimentally determined from measurements on a UV–visible spectroradiometer (Optronic OL-50 series 750 equipped with an OL 740-70 integrating sphere reflectance attachment). In Fig. 5a, the absorbed radiation fractions for different number of layers are presented; it can be seen that, starting from one to four layers of catalyst, the absorbed fraction can be noticeably increased, particularly in the range of lamp emission peak (not shown here) at approximately 350 nm.

Results of the absorbed radiation fraction are used to compute the overall radiation interchange with the model [Eq. (13)]. The $e^{a,sup}$ averaged on the y' direction for the four cases, is depicted in Fig. 5b. The obtained profiles show that, when more deposition cycles are made, more radiation is absorbed and available for reaction. However, this increment is progressively reduced with the number of layers. Comparing the absorbed radiation with that obtained for one layer, there is a 13% increase with two layers, a 6.8% increase with three layers and a 3.6% when a fourth layer is added. Therefore, the experimental study was conducted with four layers of catalyst.
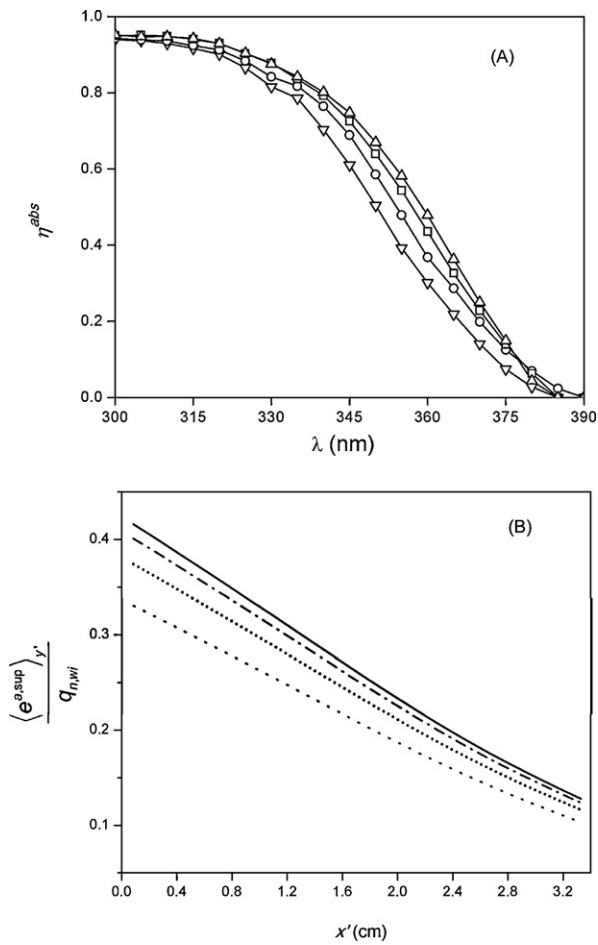
Fig. 5. (A) Spectral absorbed radiation fraction of catalyst. Key: ($\triangledown$) 1 layer; ($\bigcirc$) 2 layers; ($\square$) 3 layers; ($\triangle$) 4 layers. (B) Relative absorbed radiation for different number of catalyst layers. Key: (— –) 1 layer; (······) 2 layers; (—·—) 3 layers; (——) 4 layers.
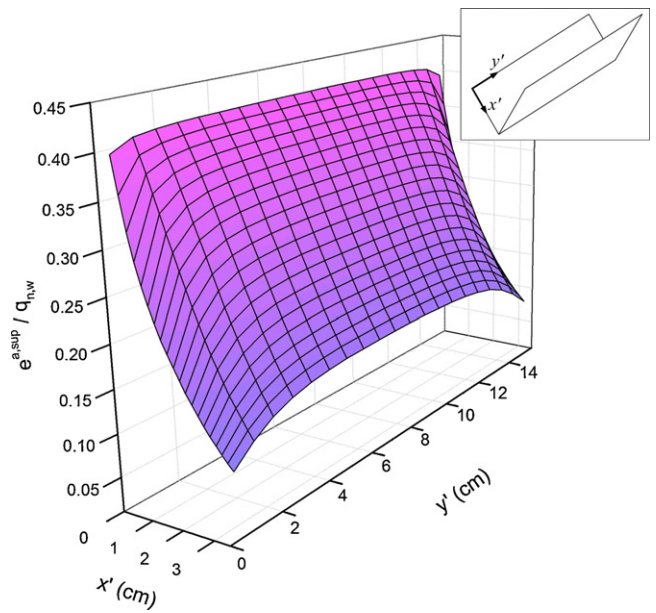

Fig. 6. Relative absorbed radiation on a catalytic plate.

The relative absorbed radiation $\left(e^{a,\text{sup}}(x', y')/q_{n,\text{wi}}\right)$ over a plate of a photocatalytic triangular channel is depicted in Fig. 6, where x' and y' are spatial variables that correspond to a coordinate system mounted on the catalytic plate.

4.3. Model and experimental results

A virtual model for the corrugated reactor geometry was designed with Gambit® software. The domain was meshed with an unstructured grid and separated into two types of zones according to their behavior regarding reaction rate and flow.
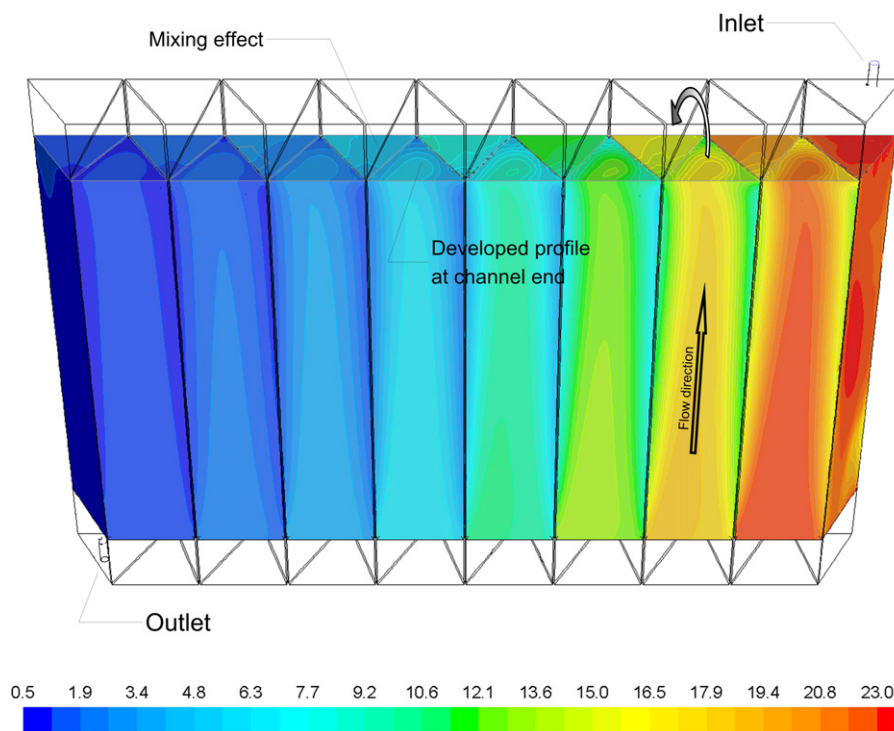

Fig. 7. HCHO concentration (ppmv) for a typical run. C_F^{in}: 24.1 ppmv; RH: 50%; radiation level: 100%.
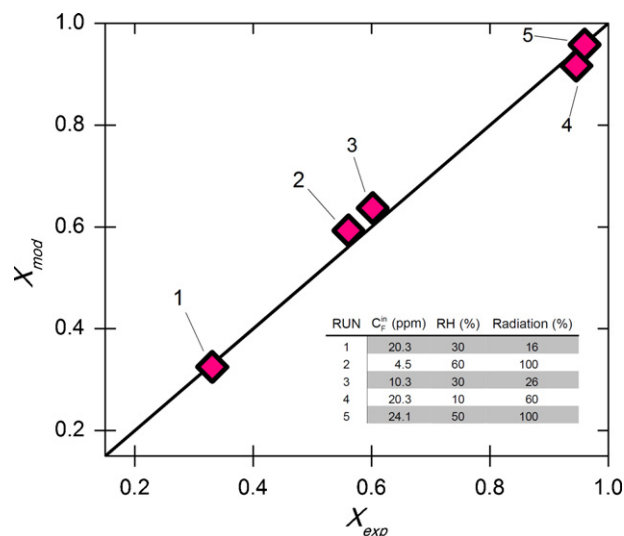
Fig. 8. Comparison of model and experimental conversions.

Type I zones are the triangular prisms with two catalytic walls where the pollutant elimination takes place. These zones were meshed with hexahedral cells aligned with the main direction of the channel. Type II zones are non reactive volumes that connect type I zones: entrance, "elbows" and exit, in which all of the walls are not reactive. These subdomains were meshed with tetrahedral elements in a finer mesh.

The resolution of the complete set of governing equations was achieved in Fluent 12. The radiation modeling was developed externally and introduced into the software as custom functions. These functions included the heterogeneous reaction rate and the absorption behavior of each catalytic surface. In this manner, the software solves the momentum and species balances subject to the imposed boundary conditions.

Computational results for the complete velocity, radiation and species fields inside the reactor were obtained. A typical HCHO concentration field is shown in Fig. 7. The picture shows a decreasing concentration along the reactor pathway. The effect of the catalytic walls is appreciable along each channel. It is also clear that the change in direction from one channel to the other acts as a static mixer, renewing the concentration profile of HCHO.

The simulation of the corrugated reactor was made for five operating conditions with different inlet concentrations of reactants, relative humidity and radiation levels. These conditions were experimentally tested in the constructed bench scale photocatalytic reactor, for which the inlet and outlet HCHO concentrations were determined. Overall conversions from the model simulations were contrasted to the experimental results. The comparison is depicted in Fig. 8; the straight line does not represent a linear regression, but an ideal match between model and experiments. Good agreement was found between simulation results and experimental data. The root mean square error, based on the experimental and predicted HCHO conversions, was lower than 4%.

5. Conclusions

A methodology has been described and applied to scale-up photocatalytic wall reactors, from a simple geometry, laboratory scale photoreactor operated under kinetic control regime to a corrugated plate type coated with TiO_2 as catalyst. Two different size and configuration reactors were designed, constructed and modeled, based on the fundamentals of reaction engineering, radiation transport theory and computational aids.

Results showed that the kinetic expression obtained was independent of the chosen reactor geometry and size. The methodology, based on the computation of view factors for modeling radiation interchange, was validated with experimental runs in the corrugated reactor. The use of CFD allowed the simulation and resolution of velocity and concentrations fields in a complex geometry reactor that otherwise would have been more difficult to achieve. The results of the formaldehyde overall conversion showed good agreement between model predictions and experiments, with a root mean square error of less than 4%. Consequently, the employed methodology can be applied for scaling-up other types of photoreactors with different sizes and/or configurations.

Acknowledgements

References

[1] A.P. Jones, Indoor air quality and health, Atmos. Environ. 33 (1999) 4535–4564.
[2] Y. Lu, D. Wang, C. Ma, H. Yang, The effect of activated carbon adsorption on the photocatalytic removal of formaldehyde, Build. Environ. 45 (2010) 615–621.
[3] F. Shiraishi, D. Ohkubo, K. Toyoda, S. Yamaguchi, Decomposition of gaseous formaldehyde in a photocatalytic reactor with a parallel array of light sources. 1. Fundamental experiment for reactor design, Chem. Eng. J. 114 (2005) 153–159.
[4] L. Wang, M. Sakurai, H. Kameyama, Study of catalytic decomposition of formaldehyde on Pt/TiO_2 alumite catalyst at ambient temperature, J. Hazard. Mater. 167 (2009) 399–405.
[5] B. Hanoune, T. Lebris, L. Allou, C. Marchand, S. Lecalve, Formaldehyde measurements in libraries: comparison between infrared diode laser spectroscopy and a DNPH-derivatization method, Atmos. Environ. 40 (2006) 5768–5775.
[6] A. Blondel, H. Plaisance, Screening of formaldehyde indoor sources and quantification of their emission using a passive sampler, Build. Environ. 46 (2011) 1284–1291.
[7] N. Bruce, R. Perez-Padilla, R. Albalak, Indoor air pollution in developing countries: a major environmental and public health challenge, B. World Health Organ. 78 (2000) 1078–1092.
[8] Y. Zhang, X. Luo, X. Wang, K. Qian, R. Zhao, Influence of temperature on formaldehyde emission parameters of dry building materials, Atmos. Environ. 41 (2007) 3203–3216.
[9] IARC, Evaluation of Carcinogenic Risks to Humans: Formaldehyde, 2-Butoxyethanol and 1-tert-Butoxypropan-2-ol, Monographs of the International Agency for Research on Cancer, Lyon, France, 2006, 88.
[10] J. Peral, D.F. Ollis, Heterogeneous photocatalytic oxidation of gas-phase organics for air purification: acetone, 1-butanol, butyraldehyde, formaldehyde, and *m*-xylene oxidation, J. Catal. 136 (1992) 554–565.
[11] T.N. Obee, R.T. Brown, TiO_2 photocatalysis for indoor air applications: effects of humidity and trace contaminant levels on the oxidation rates of formaldehyde, toluene, and 1,3-butadiene, Environ. Sci. Technol. 29 (1995) 1223–1231.
[12] R.M. Alberici, W.F. Jardim, Photocatalytic destruction of VOCs in the gas-phase using titanium dioxide, The Lamp 14 (1997).
[13] G. Imoberdorf, H. Irazoqui, O. Alfano, A. Cassano, Scaling-up from first principles of a photocatalytic reactor for air pollution remediation, Chem. Eng. Sci. 62 (2007) 793–804.
[14] J.-L. Shie, C.-H. Lee, C.-S. Chiou, C.-T. Chang, C.-C. Chang, C.-Y. Chang, Photodegradation kinetics of formaldehyde using light sources of UVA, UVC and UVLED in the presence of composed silver titanium oxide photocatalyst, J. Hazard. Mater. 155 (2008) 164–172.
[15] P. Chin, L.P. Yang, D.F. Ollis, Formaldehyde removal from air via a rotating adsorbent combined with a photocatalyst reactor: kinetic modeling, J. Catal. 237 (2006) 29–37.
[16] M. Mohseni, F. Taghipour, Experimental and CFD analysis of photocatalytic gas phase vinyl chloride (VC) oxidation, Chem. Eng. Sci. 59 (2004) 1601–1609.
[17] I. Salvadó-Estivill, A. Brucato, G. Li Puma, Two-dimensional modeling of a flat-plate photocatalytic reactor for oxidation of indoor air pollutants, Ind. Eng. Chem. Res. 46 (2007) 7489–7496.

[18] S. Romero-Vargas Castrillón, H. de Lasa, Performance evaluation of photocatalytic reactors for air purification using computational fluid dynamics (CFD), Ind. Eng. Chem. Res. 46 (2007) 5867–5880.

[19] A. Queffeulou, L. Geron, E. Schaer, Prediction of photocatalytic air purifier apparatus performances with a CFD approach using experimentally determined kinetic parameters, Chem. Eng. Sci. 65 (2010) 5067–5074.

[20] NIOSH, Method 3500 – Formaldehyde by VIS, 1994.

[21] C. Passalía, M.E. Martínez Retamar, O.M. Alfano, R.J. Brandi, Photocatalytic degradation of formaldehyde in gas phase on TiO$_2$ films: a kinetic study, Int. J. Chem. React. Eng. 8 (2010).

[22] C. Passalía, O.M. Alfano, R.J. Brandi, Modeling and experimental verification of a corrugated plate photocatalytic reactor using computational fluid dynamics, Ind. Eng. Chem. Res. 50 (2011) 9077–9086.